Title

Kernel-based anatomically-aided diffuse optical tomography reconstruction

Journal

Biomedical Physics & Engineering Express, 3(5)

ISSN

2057-1976

Authors

Baikejiang, Reheman
Zhang, Wei
Zhu, Dianwen
et al.

Publication Date

2017-09-13

DOI

10.1088/2057-1976/aa87bb

Peer reviewed

Kernel-based anatomically-aided diffuse optical tomography reconstruction

Reheman Baikejiang[1], Wei Zhang[1], Dianwen Zhu[1], Andrew M. Hernandez[2], Shadi Aminololama Shakeri[2], Guobao Wang[2], Jinyi Qi[3], John M. Boone[2], Changqing Li[1,*]

[1]School of Engineering, University of California, Merced, 5200 N. Lake Rd, Merced, CA 95340
[2]Department of Radiology, University of California, Davis, Sacramento, CA 95817
[3]Department of Biomedical Engineering, University of California, Davis, Davis, CA 95616

ABSTRACT

Image reconstruction in diffuse optical tomography (DOT) is a challenging task because its inverse problem is nonlinear, ill-posed and ill-conditioned. Anatomical guidance from imaging modalities with high spatial resolution can substantially improve the quality of reconstructed DOT images. In this paper, inspired by the kernel methods in machine learning, we proposed a kernel method to introduce anatomical guidance into the DOT image reconstruction. In this kernel method, the optical absorption coefficient at each finite element node is represented as a function of a set of features obtained from anatomical images such as computed tomography (CT) images. Compared with Laplacian approaches that include structural priors, the proposed method does not require image segmentation. The proposed kernel method is validated with numerical simulations of 3D DOT reconstruction using synthetic CT data. 5% Gaussian noise was added to both the numerical DOT measurements and the simulated CT image. The proposed method was also validated by an agar phantom experiment with the anatomical guidance from a cone beam CT scan. The effects of voxel size and number of nearest neighborhood size in the kernel method on the reconstructed DOT images were studied. The results indicate that the spatial resolution and the accuracy of the reconstructed DOT images have been improved substantially after applying the anatomical guidance with the proposed kernel method comparing to the case without guidance. Furthermore, we demonstrated that the kernel method was able to utilize clinical breast CT images as anatomical guidance without segmentation. In addition, we found that the proposed kernel method was robust to the false positive guidance in the anatomical image.

Keywords: Diffuse optical tomography, Multi-modality imaging, Anatomical guidance, Kernel method

1. INTRODUCTION

Diffuse optical tomography (DOT) is a non-invasive, non-ionizing radiation biomedical imaging modality [1] that can recover the spatial distribution of tissue optical properties such as absorption and scattering coefficients [2,3]. With measurements at multiple wavelengths, DOT has the capacity of estimating hemoglobin concentrations, oxygenation level, and water content of tissues [4,5]. Its applications include, but are not limited to, brain imaging [6,7,8], breast cancer characterization [9-13], prostate cancer monitoring [14-17], and joint tissue imaging [18,19]. However, DOT suffers from low spatial resolution due to strong optical scattering in tissues. Furthermore, DOT image reconstruction is known to be a nonlinear, ill-posed and ill-conditioned problem [20].

During the last two decades, many research groups and companies have made numerous efforts to improve the spatial resolution of DOT systems. A variety of algorithms have been proposed to improve the accuracy of the inverse problem of DOT [21-33]. As one of the most popular methods to solve nonlinear least square problems, Gauss-Newton algorithm was introduced to solve the DOT image reconstruction problem iteratively [32]. Non-iterative exact reconstruction using joint sparsity had also been investigated, in which the reconstruction was based on the MUltiple SIgnal Classification (MUSIC) criterion [25]. Model resolution-based basis pursuit deconvolution method and dimensionality reduction based optimization algorithm were implemented in DOT [29, 27]. Sparse recovery methods had also been investigated by several groups with promising results for DOT image reconstruction [22, 26]. Because of the strong optical scattering from deep targets, a depth compensation algorithm, based on the maximum singular values

* Corresponding author, E-mail: cli32@ucmerced.edu, Telephone: 1 209 228 4777

(MSVs) of layered measurement sensitivities, was used to reconstruct two 3-cm-deep absorbers with acceptable position errors [24]. Regularization parameter plays an important role in DOT reconstruction. Recently, regularization parameter choice methods in DOT imaging and their performance have been investigated [31]. Furthermore, spectral constraints and wavelength optimization were also investigated to improve reconstructed DOT image quality [33]. However, despite all the efforts from different perspectives in DOT, DOT imaging itself is still inferior to the other functional imaging modalities such as functional magnetic resonance imaging (fMRI), single-photon emission computed tomography (SPECT), and positron emission tomography (PET) in terms of spatial resolution for deep targets.

To improve the spatial resolution of DOT imaging, anatomical image guided reconstruction methods were introduced. So far, there are several types of anatomical images guided DOT imaging. Pogue, Brooksby, and Zhao, et al. have, for the first time, introduced the structural guidance from magnetic resonance imaging (MRI) into the near-infrared tomographic imaging [34–36]. Ntziachristos et al. have also reported simultaneous magnetic resonance and near-infrared mammography [37, 38]. Zhu *et al.* reported optical differentiation of benign versus malignant breast masses using an ultrasound (US)-guided DOT system [39–41]. Fang *et al.* reported combined optical and X-ray tomosynthesis breast imaging [42, 43].

In general, there are two approaches to including anatomical guidance into the DOT reconstruction: hard prior method and soft prior method [44]. In the hard prior method, also known as parameter reduction, the optical properties within the same region are forced to be uniform, which results in a decrease in the total number of unknowns from the node number of the finite element mesh to the number of distinct regions segmented from the guidance images. The disadvantages of the hard prior method include its dependence on the accuracy of segmentation and a strong bias to the incomplete or incorrect structural priors. On the other hand, the soft prior method allows smooth changes of the reconstructed optical properties in each of different regions [45]. However, both hard and soft priors require region segmentation from the anatomical images, which can only be performed by a radiologist or an expert of image processing. To eliminate the need for image segmentation, a direct regularization method in which the anatomical image gray-scale values are used to construct the regularization matrix was introduced [46–48].

In this paper, inspired by the kernel method of PET image reconstruction [49], we introduce the kernel method based image reconstruction as a new approach to include anatomical guidance into DOT reconstruction. Compared with the conventional hard and soft prior approaches, the proposed kernel method does not require target region segmentation. Compared with a direct regularization method proposed in Refs. [46,50], instead of utilizing single pixel intensities corresponding to the finite element nodes, we also use neighboring voxels, which allows us capture more structural information from the anatomical image. Furthermore, the kernel-based image model is directly incorporated into the forward model of DOT, instead of including it in the regularization term. In this study, we only consider the absorption coefficient contrast between the target and the background for simplification. In the proposed kernel method, the absorption coefficient at a node i is represented by a function of a set of features, $\boldsymbol{f}_i$, which is directly extracted from the voxel intensities of the corresponding anatomical images. Then, the kernelized DOT image model is incorporated into the forward model of DOT.

The rest of this paper is organized as follows. We introduce the kernel method, the setup of numerical simulations and phantom experiments in section 2. Then, we report the results of numerical simulation and phantom experiments to validate the kernel method in section 3. Finally, we conclude this paper in section 4 with discussions.

2. METHODS

2.1 Kernel-based anatomically-aided reconstruction algorithm

In the inverse problem of DOT, the objective function Ω, which minimizes the difference between modeled data (obtained from the forward model of DOT) and the measurements, if we only reconstruct absorption coefficients, can be written as:

$$\Omega(\boldsymbol{\mu}_a) = \frac{1}{2}\left|\left|\boldsymbol{y} - F(\boldsymbol{\mu}_a)\right|\right|_2^2 \tag{1}$$

where $\boldsymbol{\mu}_a$ is the optical absorption coefficient and $F(\boldsymbol{\mu}_a)$ is the prediction from the DOT forward model. Here we present the Gaussian kernel method that encodes anatomical information in the DOT image reconstruction. This can be accomplished by defining a kernel function for each finite element node. The optical absorption coefficient at a node i can then be written as a linear combination of kernels in a way similar to for PET [49,51,52],

$$\boldsymbol{\mu}_{a_i} = \sum_j \alpha_j \kappa(\boldsymbol{f}_i, \boldsymbol{f}_j) \tag{2}$$

where $\boldsymbol{f}_i$ and $\boldsymbol{f}_j$ are feature vectors corresponding to the finite element node i and j from anatomical image, respectively. $\kappa(\boldsymbol{f}_i, \boldsymbol{f}_j)$ is the (i, j) element $\boldsymbol{K}_{ij}$ of the kernel matrix $\boldsymbol{K}$ defined in Eq. (3).

The anatomical feature vectors are directly extracted from the corresponding voxels in the 3-dimensional (3D) anatomical images for each finite element node. Usually, DOT images are reconstructed on a finite element mesh (FEM) with a number of FEM nodes and the anatomical guidance images are displayed in voxels. Thus, the feature vector indicates the gray scale values of voxels surrounding the corresponding FEM node. For instance, if we only consider voxel neighbors (3×3×3), we have 27 voxels corresponding to each FEM node. Gray scale values of those 27 voxels are defined as one feature vector for the specific FEM node. Then, we will have one feature vector for each FEM node i indicated as $\boldsymbol{f}_i$.

The finite element mesh and the anatomical images should be co-registered. It is also worth noting that the voxels corresponding to finite element nodes on the surface of the mesh and outside of the mesh are excluded from the feature vector extraction. The vector $\boldsymbol{\alpha}$ in Eq. (2) is referred to as the coefficient image to be reconstructed. There are a variety of choices of the kernel function κ [51, 53]. Here we use the radial Gaussian kernel [54],

$$\boldsymbol{K}_{ij} = \begin{cases} exp\left(\frac{-\left|\left|\boldsymbol{f}_i - \boldsymbol{f}_j\right|\right|^2}{\sigma^2}\right), & \boldsymbol{f}_j \in knn \text{ of } \boldsymbol{f}_i \\ 0, \quad otherwise \end{cases} \tag{3}$$

where *knn* indicates the k-nearest neighbors as defined in Ref. [54]. To find k similar neighbors for each feature vector, a *knn* search was carried out using the *knnsearch* function in MATLAB according to Euclidean distance between the feature vectors, not the physical distance among the finite element nodes in the Cartesian coordinates. In this study, three different values of k (16, 32, 64), the number of nearest neighbors, were studied. Only those elements corresponding to the k-nearest neighbors were kept in the kernel matrix and the rest of them were set to be 0. The parameter σ in Eq. (3) controls the edge sensitivity. The above kernel function can be written in a matrix-vector form as

$$\boldsymbol{\mu}_a = \boldsymbol{K}\boldsymbol{\alpha} \tag{4}$$

By substituting Eq. (4) into Eq. (1), the kernelized objective function is obtained as

$$\Omega(\boldsymbol{\alpha}) = \frac{1}{2}\left|\left|\boldsymbol{y} - F(\boldsymbol{K}\boldsymbol{\alpha})\right|\right|_2^2 \tag{5}$$

When $\boldsymbol{K}$ is an identity matrix, the above equation equal to the original objective function (1). By finding partial derivative of the objective function on $\boldsymbol{\alpha}$ and setting it equal to zero:

$$\frac{\partial \Omega}{\partial \boldsymbol{\alpha}} = \boldsymbol{K}^T\boldsymbol{J}^T\boldsymbol{\delta} = 0 \tag{6}$$

where $\boldsymbol{\delta}$ is the data-model misfit, $\boldsymbol{\delta} = \boldsymbol{y} - F(\boldsymbol{K}\boldsymbol{\alpha})$, $\boldsymbol{J}$ is the Jacobian matrix, and T is the matrix transpose operator. Using the Taylor expansion of $F(\boldsymbol{K}\boldsymbol{\alpha})$ around $\boldsymbol{\alpha}_{n-1}$, we have:

$$F(\boldsymbol{K}\boldsymbol{\alpha}_n) = F(\boldsymbol{K}\boldsymbol{\alpha}_{n-1}) + \boldsymbol{J}\boldsymbol{K}\Delta\boldsymbol{\alpha}_n + \cdots \tag{7}$$

where $\Delta\boldsymbol{\alpha} = \boldsymbol{\alpha}_n - \boldsymbol{\alpha}_{n-1}$. Rewriting $\boldsymbol{\delta}$ and utilizing the first two terms of Eq. (7) (ignoring the rest, equivalently linearizing the problem) gives us

$$\boldsymbol{\delta}_n = \boldsymbol{y} - F(\boldsymbol{K}\boldsymbol{\alpha}_n) = \boldsymbol{y} - F(\boldsymbol{K}\boldsymbol{\alpha}_{n-1}) - \boldsymbol{J}\boldsymbol{K}\Delta\boldsymbol{\alpha}_n = \boldsymbol{\delta}_{n-1} - \boldsymbol{J}\boldsymbol{K}\Delta\boldsymbol{\alpha}_n \tag{8}$$

Rewrite Eq. (6) for the n^{th} iteration, we get

$$\boldsymbol{K}^T\boldsymbol{J}^T\boldsymbol{\delta}_n = 0 \tag{9}$$

Substitute Eq. (8) into Eq. (9), we have:

$$\boldsymbol{K}^T\boldsymbol{J}^T(\boldsymbol{\delta}_{n-1} - \boldsymbol{J}\boldsymbol{K}\Delta\boldsymbol{\alpha}_n) = 0 \tag{10}$$

Further simplification leads to an update equation:

$$[\boldsymbol{K}^T\boldsymbol{J}^T\boldsymbol{J}\boldsymbol{K}]\Delta\boldsymbol{\alpha}_n = \boldsymbol{K}^T\boldsymbol{J}^T\boldsymbol{\delta}_{n-1} \tag{11}$$

Since the matrix $\boldsymbol{K}^T\boldsymbol{J}^T\boldsymbol{J}\boldsymbol{K}$ is ill-conditioned, a diagonal term (the Tikhonov regularization) is added to stabilize the inverse problem. In this case the update equation becomes:

$$[\boldsymbol{K}^T\boldsymbol{J}^T\boldsymbol{J}\boldsymbol{K} + \lambda\boldsymbol{I}]\Delta\boldsymbol{\alpha}_n = \boldsymbol{K}^T\boldsymbol{J}^T\boldsymbol{\delta}_{n-1} \tag{12}$$

After the coefficient image $\boldsymbol{\alpha}$ is reconstructed, the desired absorption coefficient image can be calculated as

$$\boldsymbol{\mu}_a = \boldsymbol{K}\boldsymbol{\alpha} \tag{13}$$

2.2 Soft prior method

We compare the proposed kernel method with the soft prior method in this study. Here we describe the soft prior method briefly. The objective function (Ω), which minimizes the difference between the modeled data (obtained from forward model) and the measurements, if we only reconstruct the absorption coefficients, can be written as

$$\Omega(\boldsymbol{\mu}_a) = \left|\left|\boldsymbol{y} - F(\boldsymbol{\mu}_a)\right|\right|_2^2 + \lambda\left|\left|L(\boldsymbol{\mu}_a - \boldsymbol{\mu}_{a_0})\right|\right|_2^2 \tag{14}$$

Here λ is the regularization parameter and L is a dimensionless penalty matrix which can be obtained from other structural imaging modalities such as CT. The L matrix is calculated before the reconstruction without further change. This type of inclusion of priori information is often referred as soft-priors [44, 45]. In Laplacian-type, the L matrix is a matrix that relates each nodal property of the numerical model to all other nodes. Therefore given a node i within the mesh, its relationship to another node j having Laplacian structure within the same mesh can be given as [35],

$$\boldsymbol{L}_{ij} = \begin{cases} 1, & i = j \\ -\frac{1}{N}, & i \text{ and } j \text{ are in the same region} \\ 0, & \text{otherwise} \end{cases} \tag{15}$$

where N is number of finite element nodes comprising a given region. In this case, $\boldsymbol{L}^T\boldsymbol{L}$ approximates a second-order Laplacian smoothing operator within each region, and works to average the update within the same region, while allowing discontinuity among different regions.

2.3 Numerical simulation

2.3.1 Optimization of the Kernel method

The voxel number for each corresponding node and the number of nearest neighbors in *knnsearch* are important parameters in constructing kernel matrix $\boldsymbol{K}$ and have significant effects on the kernel method. In this paper, we studied four different voxel numbers, 3×3×3, 5×5×5, 7×7×7, and 9×9×9. The lengths of the feature vector were 27, 125, 343, and 729, respectively. For *knnsearch*, three different values of k (16, 32, 64), the number of nearest neighbors, were also studied. To evaluate and compare the quality of the reconstructed DOT images quantitatively, we used a combination of 4 metrics listed below. Their detailed definitions can be found in Ref. 55. They are volume ratio (VR), Dice similarity coefficient (Dice), contrast-to-noise ratio (CNR), and mean square error (MSE). In general, for a reconstructed image to have better quality, it has a VR and Dice close to one, a small MSE, and a large CNR [56].

In the numerical simulations, we used a cylindrical phantom with a diameter of 78 mm and a height of 60 mm. A cylindrical target (diameter of 10 mm and height of 10 mm) was placed at 15 mm away from the center line of the phantom and 20 mm below the top surface of the phantom in the vertical direction as depicted in Fig. 1(a). The numerical phantom was discretized into a 3D tetrahedral finite element mesh with 9,877 nodes, 54,913 elements, and 2,921 surface nodes. Numerical DOT measurement data at six angular projections were generated by the DOT forward model in continuous wave mode [57]. In each angular projection, six source positions separated 5 mm apart were placed on one side of the phantom in the vertical line as indicated by the black dots in Fig. 1(b). A rectangular region on the opposite side of the numerical phantom was chosen to be the field of view (FOV) and all surface nodes within this region were used as measurement detectors as indicated by the red dots in Fig. 1(b). Then, 5% Gaussian noise (signal to noise ratio (SNR) of 36.85 dB) was then added to the numerical DOT measurement data. The reduced optical scattering coefficient was set to 1 mm^{-1} for both target and background uniformly. The optical absorption coefficient was 0.007 mm^{-1} for phantom background and 0.028 mm^{-1} for the target as shown in Table 1.

A synthetic 3D CT image with a matrix size of 527×527×401 was generated with a an isotropic voxel size of 0.15 mm as shown in Fig. 1(c). The voxel intensities of the target region and the background were set to 1.5 and 0.34,

respectively, which are close to the CT image intensity in the phantom experiments described below. 5% Gaussian noise (SNR of 36.85 dB) was also added to the synthetic CT images.

2.2.2 CT contrast effect in the kernel method for CT guided DOT reconstruction

The voxel intensity in the CT image is used to generate the kernel matrix and therefore further analysis is required to assess how the ratio of the target pixel intensity to the background pixel intensity affects the performance of the proposed kernel method. For this purpose, 3 more synthetic CT images with different CT contrasts were used for the kernel method with $k = 64$ and voxel number of 9×9×9. In these simulations, the background voxel intensity of the CT image was set to be uniform as 0.34. For the target region, voxel intensity values of 0.68, 1.02 and 2.04 were used for the contrast ratios of 1:2, 1:3, and 1:6, respectively. For these three cases, all other factors such as the phantom geometry and optical properties were the same as described in the above section.

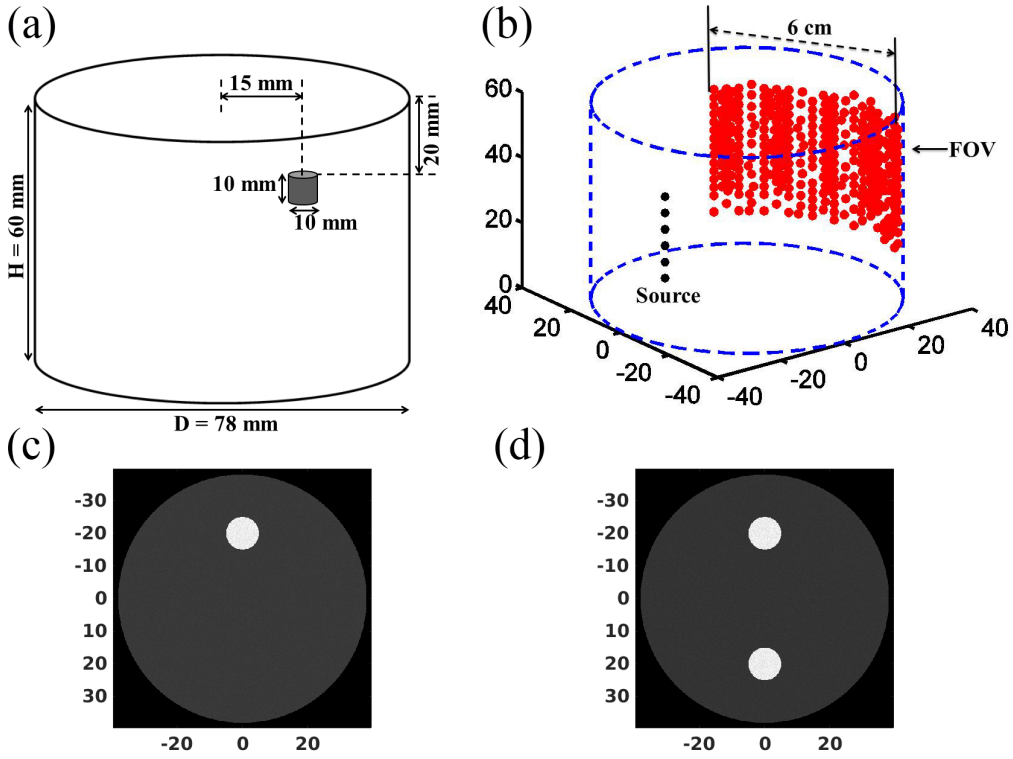

Figure 1. (a) Phantom geometry. (b) Source nodes (black) and detector nodes (red) in a 6 cm wide measurement patch for an angular projection. (c) One cross section of simulated CT image with 5% Gaussian noise. (d) The CT image with a true target (top) and a false positive target (bottom) used for the anatomical guidance in the false positive simulation.

Table 1. Optical properties and geometry dimensions of the phantom for the numerical simulation.

	Diameter	Height	μ_a	μ_s'
Background	78.0 mm	60.0 mm	0.007 mm^{-1}	1.0 mm^{-1}
Target	10.0 mm	10.0 mm	0.028 mm^{-1}	1.0 mm^{-1}

2.3.3 Effect of false positive guidance in the kernel method

A false positive target in the synthetic CT image (see Fig. 1d) was used to investigate how false positive guidance affects the proposed kernel method. For this purpose, the top target is the true optical absorption target and the bottom target is the false optical absorption target. Both targets were defined with the same contrast and size in the CT image. In this numerical simulation, all other factors were the same as described in section 2.3.1.

2.3.4 Clinical breast CT image as anatomical guidance in the kernel method

The ultimate goal of the proposed kernel method in CT guided DOT is the applications in the clinical studies. Compared with the phantom CT image, a breast CT image has much more heterogeneous background and different CT contrast. In this study, a clinical breast CT image as shown in Fig. 2(a) was used, in which the CT image at different coronal planes of the breast is plotted. This CT data set is from a 48-year old women presented for diagnostic workup of a palpable lump in the left breast at the one o'clock position. On mammography, she was found to have heterogeneously dense breast tissue and a mostly obscured 2 cm mass corresponding to the palpable finding. As part of a clinical trial, the patient underwent a contrast-enhanced dedicated breast CT scan 103 seconds after the injection of 100 mL of Visipaque 320 at a rate of 4 mL/sec. On the contrast-enhanced breast CT image as shown in Fig. 2(a), the oval 20x24x17mm (APxMLxSI) mass becomes conspicuous. The histopathology showed a low-grade infiltrating mammary carcinoma, which was estrogen and progesterone receptor positive and Her-2, negative. We have performed segmentation of the breast CT image and display the segmented image in Fig. 2(b), where the highlight region is the oval mass and the grey region is the background. The segmentation was used in the soft prior method for anatomical guidance.

When the patient was scanned on the breast CT scanner, there was no optical imaging system. In this study, optical measurements were simulated with the forward model previously-reported by our group (Ref. 57). From the CT image, a 3D finite element mesh was generated with 27,146 tetrahedral elements, 6,187 nodes, as displayed in Fig. 2(c). Similar to the numerical phantom studies, numerical measurements in six angular projections were used with an angular step of 60 degrees. For each angular projection, we selected a patch with a width of 6 cm and a height of 4 cm to mimic the FOV of a CCD camera, as shown in Fig 2(d). All the surface nodes in the patch were used as DOT detectors. For each angular projection, we selected 6 nodes at the opposite side of the patch as the laser illumination position. The laser illumination position had an interval of 0.5 cm. The laser beam illuminated the six positions sequentially. For each illumination position, the light intensities on the detectors in the FOV were recorded as the measurements. With six angular projections, we have 36 laser source positions and 14,082 total measurements. We added 5% Gaussian noise (SNR of 36.85 dB) onto the numerical DOT measurement data. In the forward model, we have set the nodes in the target region with the optical absorption coefficient of 0.028 mm^{-1} and the reduced scattering coefficient of 1.0 mm^{-1}. The nodes in the background region had the optical absorption coefficient of 0.007 mm^{-1} and the reduced scattering coefficient of 1.0 mm^{-1}.

During the DOT reconstruction, for the kernel, we used the breast CT image (Fig. 2a) without segmentation as the anatomical guidance to generate the kernel matrix $\boldsymbol{K}$. For the soft prior method, we had to segment the breast CT image (as shown Fig. 2b) because the finite element nodes in the target region and the background should be known to generate the regularization matrix $\boldsymbol{L}$ in the soft prior method [45].

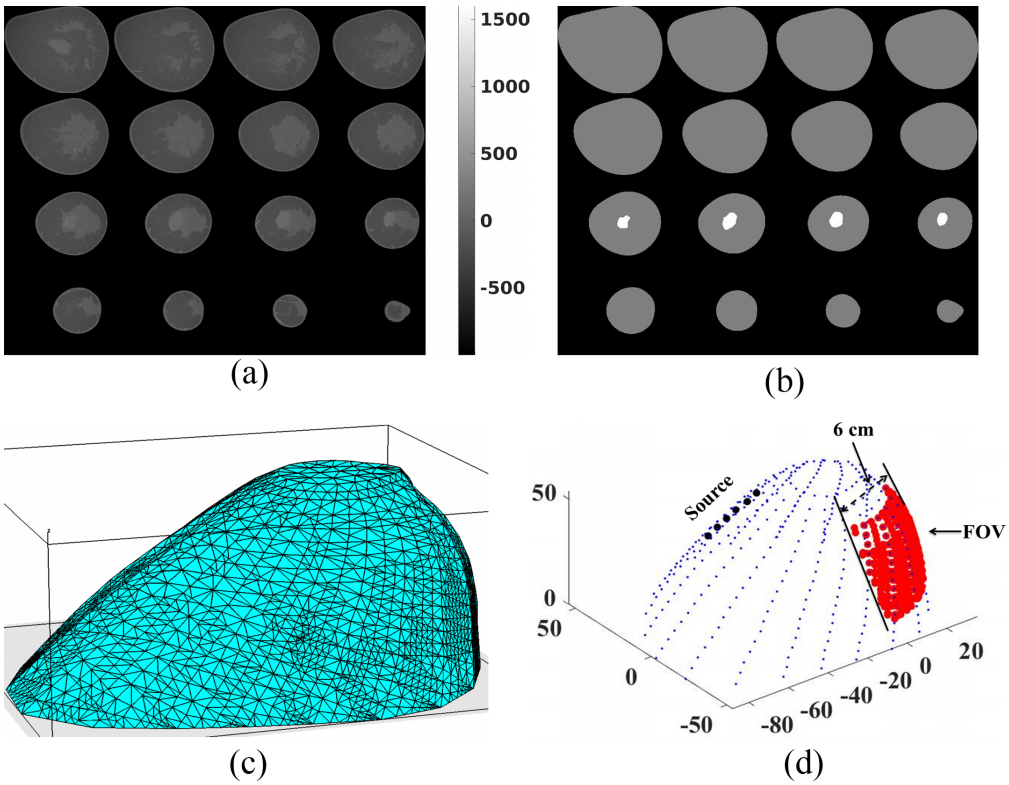

Figure 2. (a) Transverse sections of the CT image of a breast cancer patient. (b) The segmentation of the CT image shown in (a) where the tumor is highlighted. (c) The finite element mesh of the breast for DOT reconstruction. (d) The laser illumination positions (black dots) and the detector nodes (red dots) of a typical angular projection.

2.4 Phantom experimental setup

In the phantom experiment, we used a cylindrical phantom with a diameter of 78 mm and a height of 60 mm that was made of 2% Agar, titanium dioxide (TiO_2) as scattering particles, Indian ink as an optical absorber, and water. A jelly-like agar phantom was fabricated with a through hole at the target location, which was 19.82 mm away from the center line of the cylinder. A cylindrical target with a diameter of 10.86 mm and a height of 13.63 mm was made inside a transparent glass tube with a wall thickness of 0.3 mm. Then, the target inside the glass tube was inserted into the hole of the background phantom. The center of the target was 19.82 mm away from the center of the base phantom, which was calculated from the CT image. The top 20 mm and the bottom 30 mm of the hole were filled with same material as the base phantom (Fig. 3a). The base phantom was fabricated to have μ_a =0.007 mm^{-1} and μ_s'=1.0 mm^{-1} at the wavelength of 650 nm. The target had an optical absorption coefficient of 0.028 mm^{-1} and a reduced scattering coefficient of 1.0 mm^{-1} at the wavelength of 650 nm as listed in Table 2.

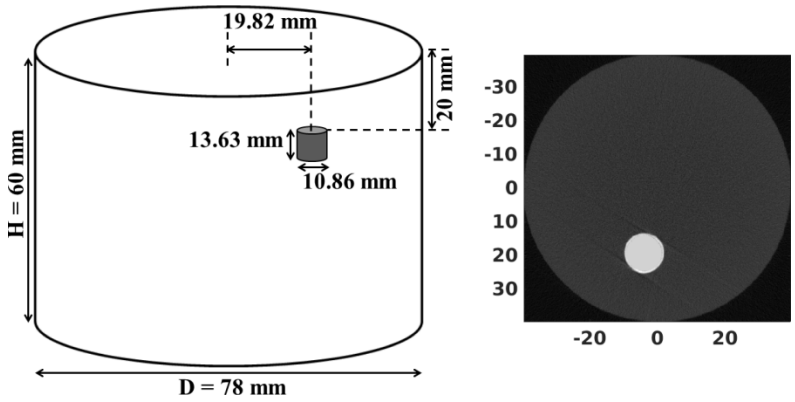

Figure 3. (a) Phantom geometry. (b) One slice CT image of phantom in experiment.

We used the same finite element mesh as that in the numerical simulation to discretize the agar phantom. The experimental measurement data were acquired with a DOT prototype system built in our lab that consisted of an EMCCD camera (C9100-13,Hamamatsu) with a lens (Schneider Xenon 25mm f /0.95), a diode laser at 650 nm with a collimator (BWF-OEM-650-200-100-0.22, B&W Tek, Inc), a linear stage (XN10-0060-E01-71 C044289, Velmex, Bloomfield,NY), and a rotary stage (B4872TS-ZRS C042679, Velmex, Bloomfield,NY). Details of the prototype DOT imaging system were described in Ref. 57. During the experiments, the EMCCD camera stayed stationary while the rotary stage rotated the phantom with an angular step of 60 degrees. For each rotation angle, the linear stage moved the laser beam six steps in the vertical direction with a step size of 5 mm. For each illumination position, an image was taken by the EMCCD camera and mapped onto the detector nodes within the measurement patch as depicted in Fig. 1(b). This experimental setup generated the same source-detector pairs as those in the numerical simulation. Measurements are obtained in the continuous wave mode and were calibrated with a homogeneous phantom by the same approach as described in Ref. 58.

A CT volume data set with a matrix size of 470×470×368 and an isotropic voxel size of 0.169 mm was reconstructed using 500 projections acquired on a dedicated breast CT system. Details of the breast CT system were described in Ref. 59. Briefly, the x-ray tube was operated at a current of 160 mA and a voltage of 50 kVp with 0.15 mm of added copper (Cu) filtration. 500 angular projections were acquired. A filtered back-projection algorithm was used to reconstruct the CT image with a Shepp-Logan filter. A coronal slice of the reconstructed CT data set used to calculate the target's size and position is shown in Fig. 3(b). Because the optical absorption contrast alone does not have CT contrast, and only the glass tube was observed in the reconstructed CT images, we filled the target regions by pixels having the same CT contrast as the glass tube to provide anatomical guidance in the kernel method. The mean voxel intensities of the target region and the background were 1.50 and 0.34, respectively.

Table 2. Optical properties and geometry dimensions of the phantom for experiment.

	Diameter	Height	μ_a	μ_s'
Background	78.0 mm	60.0 mm	0.007 mm^{-1}	1.0 mm^{-1}
Target	10.86 mm	13.63 mm	0.028 mm^{-1}	1.0 mm^{-1}

3. RESULTS

3.1 Numerical Simulation Results

3.1.1 Optimization of the kernel method

Numerical simulation with one target was conducted to evaluate the proposed kernel method. The geometric and optical properties of the numerical phantom are described in section 2.3.1. Fig. 4(a) shows transverse sections of the ground truth optical absorption coefficient image of the simulation phantom. Numerical measurements were generated by the DOT forward model as described in section 2.3.1. First, for comparison, we reconstructed the DOT image by the Levenberg-Marquardt algorithm with the CT structural guidance through the approaches of the soft prior and without any structural guidance, respectively [45]. The reconstructed absorption coefficient image is plotted in Fig. 4(b) for the

case without the structural prior and Fig. 4(c) for the soft prior method. Fig. 4(b) indicates that the reconstructed absorption coefficient in the target region is nearly half of its true value we assigned in the simulation, and there are strong artifacts near the bottom and top boundaries of the cylindrical phantom. With the soft prior method, we can reconstruct very good absorption coefficient image with accurate target size and absorption coefficient in the target region as shown in Fig.4 (c), which is consistent with our previous studies [57,60]. Then, we performed the DOT reconstruction with the proposed kernel method. To investigate how the parameters in the kernel method affect the DOT reconstruction, we studied four different voxel numbers (3×3×3, 5×5×5, 7×7×7, and 9×9×9) and three different nearest neighbors (k=16, 32, 64) with 12 combinations of the kernel method based DOT reconstructions. Reconstructed DOT images with a fixed voxel number (3×3×3) and three different k of 16, 32, 64 are plotted in the middle row of Fig. 4, from which we find that k = 64 outperformed the cases with k=16 and k=32. The bottom row of Fig. 4 shows the reconstructed DOT images with the kernel method for a fixed k=64 and different voxel numbers of 5×5×5, 7×7×7, and 9×9×9. From these figures, it is seen that the qualities of the reconstructed DOT images are slightly improved by increasing the number of voxel for the kernel method.

To evaluate the simulation results quantitatively, we calculated the image quality metrics such as VR, Dice, CNR, and MSE for the reconstructed DOT images in Fig. 4 for the cases of without the anatomical guidance case (Tikhonov regularization alone), with the soft prior method, and the six combinations of the kernel method. We have listed the quantitative image quality metrics in Table 3, which indicates that the reconstruction with the soft prior method is the best with both VR and Dice coefficients of 1 and the lowest recorded MSE. We also see that the DOT reconstruction without any structural guidance is the worst with the VR of 1.19, which indicates that the reconstructed target size is larger than the exact size because of blurring effects from optical scattering. Dice and CNR coefficients are smaller than those with the soft prior method. For the cases with the kernel method, MSE decreased nearly linearly when k and voxel number increased. Reconstructed DOT image for k=64 and voxel number of 7×7×7 is the best among all the cases of the kernel method with the highest CNR of 32.51 and the lowest MSE of 3.26e-07. VR and Dice coefficients are the same for all the combinations of the kernel method, except for the case k=16 and voxel number of 3×3×3 with the lowest VR of 0.47 and Dice of 0.64.

3.1.2 CT contrast effect in the kernel method for CT guided DOT reconstruction

The reconstructed optical absorption coefficient images with the kernel method when k=64 and voxel number of 7×7×7 are plotted in Figs, 5a, 5b, and 5c for the CT contrast of 2:1, 3:1, and 6:1, respectively. Fig. 5 indicates that the reconstructed images are similar to those in the previous simulations, in which the CT contrast is 4.4:1. The quantitative image metrics were calculated and listed in Table 4, from which we see that the metrics are also very close for these three cases, although the case with the contrast of 6:1 has slightly better CNR and MSE values, but lower VR and Dice coefficients. These results indicate that the proposed kernel method does not require a high CT contrast for its guidance in DOT reconstruction.

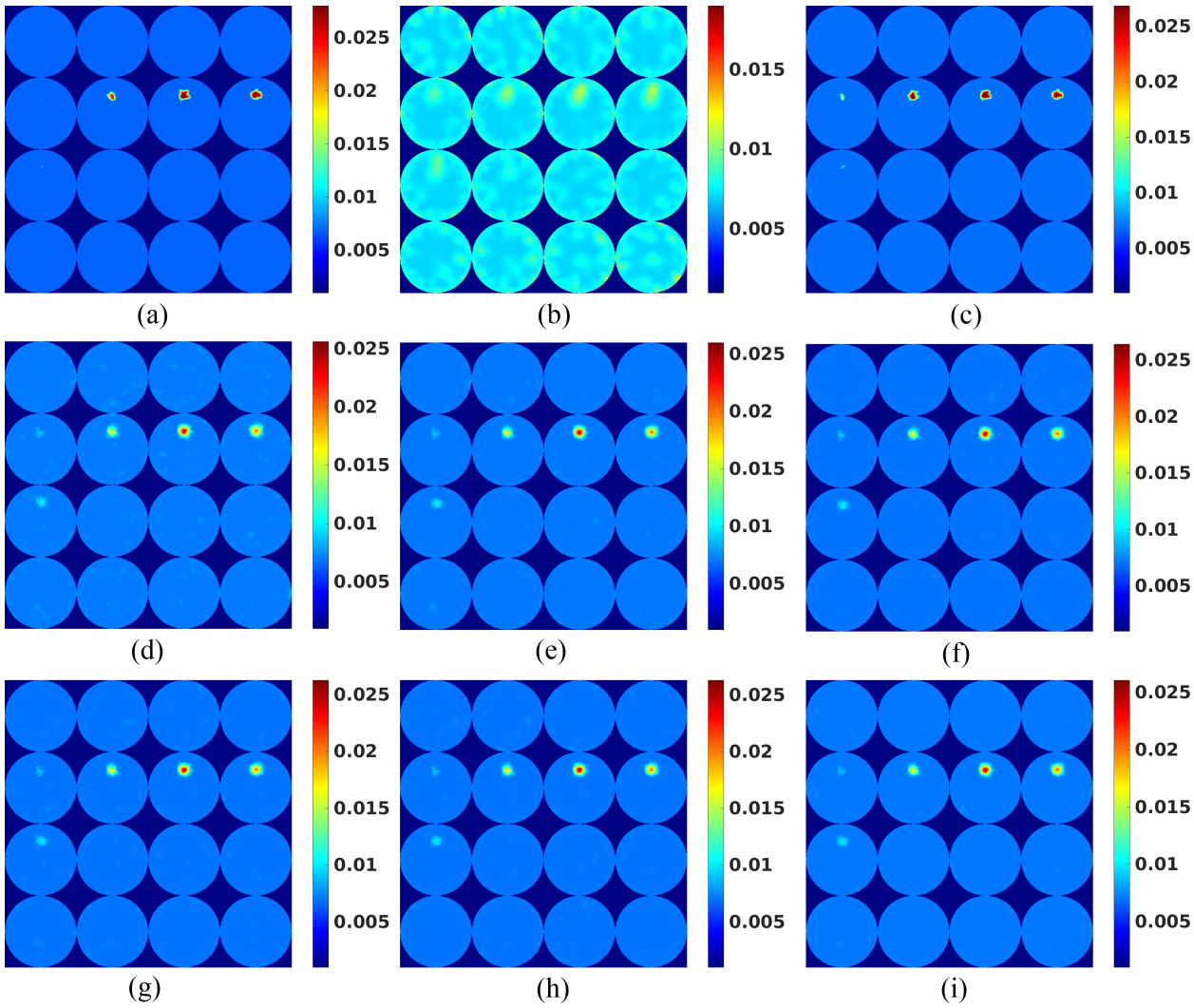

Figure 4. The absorption coefficient images for numerical simulation. (a) Ground truth image; (b) the reconstructed image without the structural prior; (c) reconstructed image with the soft prior from the CT guidance. The reconstructed absorption coefficient images with the kernel method for a fixed voxel numbers of 3×3×3 and (d) k = 16, (e) k = 32, (f) k = 64; and for a fixed k=64 with different voxel number of (g) 5×5×5, (h) 7×7×7, and (i) 9×9×9.

Table 3. For the numerical simulation, the calculated VR, Dice, CNR and MSE with the kernel method for different numbers of nearest neighbor k and different voxel numbers, with soft prior, and with no prior.

k	Voxel number	VR	Dice	CNR	MSE
16	**3×3×3**	0.47	0.64	30.35	3.51e-07
32	**3×3×3**	0.52	0.68	31.57	3.37e-07
64	**3×3×3**	0.52	0.68	32.32	3.28e-07
64	**5×5×5**	0.52	0.68	32.43	3.30e-07
64	**7×7×7**	0.52	0.68	32.51	3.26e-07
64	**9×9×9**	0.52	0.68	32.50	3.27e-07
Soft prior		1.0	1.0	891.03	3.51e-08
No prior		1.19	0.04	3.78	1.52e-06

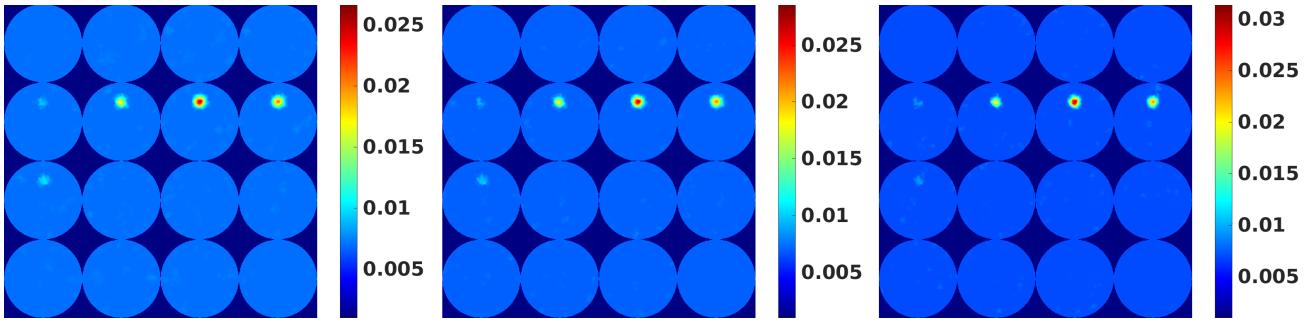

Figure 6. Reconstructed DOT images with the kernel method for a fixed voxel numbers of 7×7×7 and k = 64 with the structural guidance from the CT images of different contrasts: (a) 1:2, (b) 1:3, (c) 1:6.

Table 4. The calculated VR, Dice, CNR and MSE for the reconstructed absorption coefficient images as shown in Fig. 6 with different background to target CT contrasts.

CT Contrast	VR	Dice	CNR	MSE
1:2	0.57	0.72	33.09	3.23e-07
1:3	0.57	0.72	34.63	2.94e-07
1:6	0.47	0.65	35.33	2.68e-07

3.1.3 Effect of the false positive target in the kernel method

Using the anatomical guidance from the simulated CT image with a false positive target, we have performed the DOT reconstruction with both the soft prior and the kernel method. For the soft prior method, we have tried different regularization parameters and plotted the best reconstructed image in Fig. 6(b). For the kernel method, we used the optimized parameters as k = 64 and voxel numbers of 7×7×7 and the reconstructed optical absorption coefficient image is plotted in Fig. 6(c). Compared with the ground truth image plotted in Fig. 6(a), it is clear that there is no false positive target observed in the reconstructed DOT images when both the soft prior method and the kernel method were used as shown in Fig. 6(b) and Fig. 6(c), respectively. It is also confirmed by the profile plot (as shown in Fig. 6d) across the dotted line in Fig. 6(a). From the profile plot, it is seen that there is no false positive target for the kernel method and a negligible false positive target for the soft prior method as the slight bump in the profile plot. This indicates that the kernel method is robust to the false positive guidance in the anatomical image.

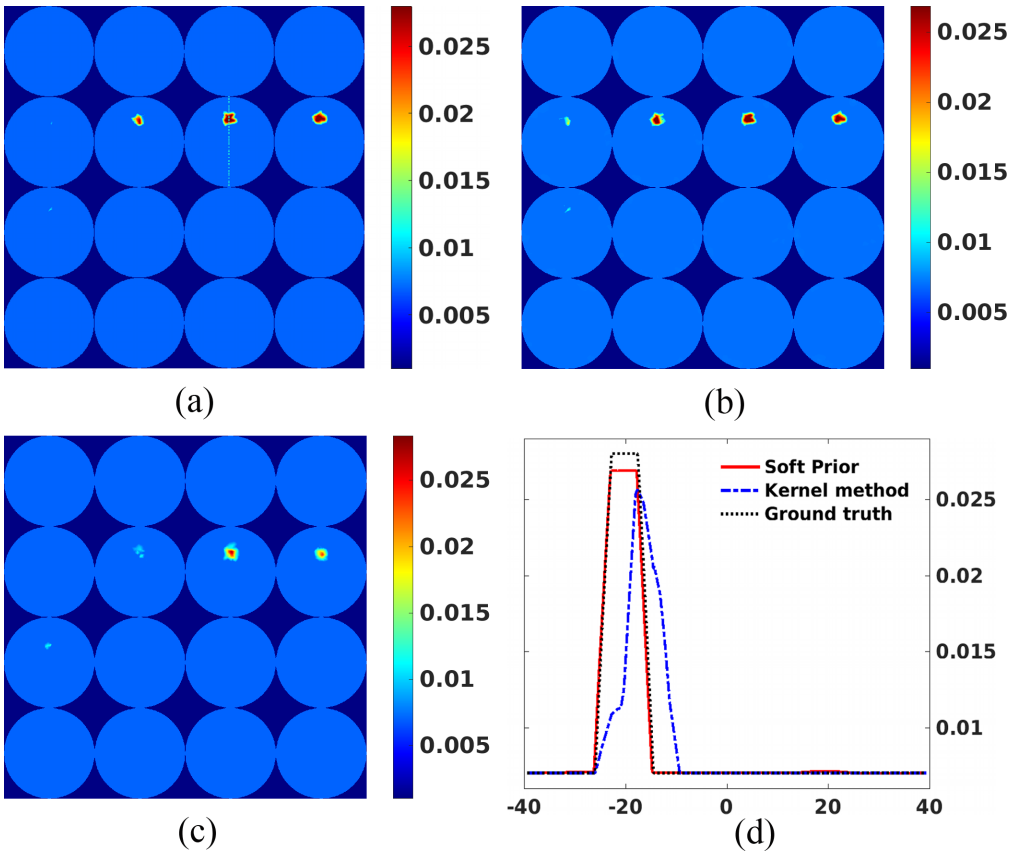

Figure 6. The absorption coefficient image: (a) the ground truth image; (b) the reconstructed image with soft prior; (c) the reconstructed image with the kernel method.

3.1.4 Clinical breast CT image as the anatomical guidance

The ground truth image is plotted in Fig. 7(a), which is generated from the segmented image of clinical breast CT image. We have also performed the DOT reconstruction without any anatomical guidance for this case and the reconstructed absorption coefficient image is plotted in Fig. 7(b), from which it is seen that the target is barely reconstructed. One possible reason is that we only used the measurements from six angular projections, which is not optimized for the DOT reconstruction without anatomical guidance. We have also reconstructed the absorption coefficient images with the soft prior method (Fig. 7c) and with the kernel method (Fig. 7d). Both methods have reconstructed the target very well. It is not surprising to see that the reconstructed target in Fig. 7(c) has a sharp boundary because the segmentation of the target was applied in the soft prior method without adding any error. With the anatomical guidance from the CT image directly without segmentation, the kernel method with k=64 and the voxel number of 7×7×7 performed well without introducing any false positive targets as shown in Fig. 7(c). We have also calculated the image quality metric to evaluate the reconstructed DOT image quantitatively and listed them in Table 5.

Table 5. For Simulation with breast CT image, the calculated VR, Dice, and CNR for images in Fig. 7

	VR	Dice	CNR	MSE
No prior	0.35	0.0	1.37	1.14e-05
Soft prior	1.0	1.0	36.78	1.06e-06
Kernel method	0.59	0.74	28.00	4.09e-07

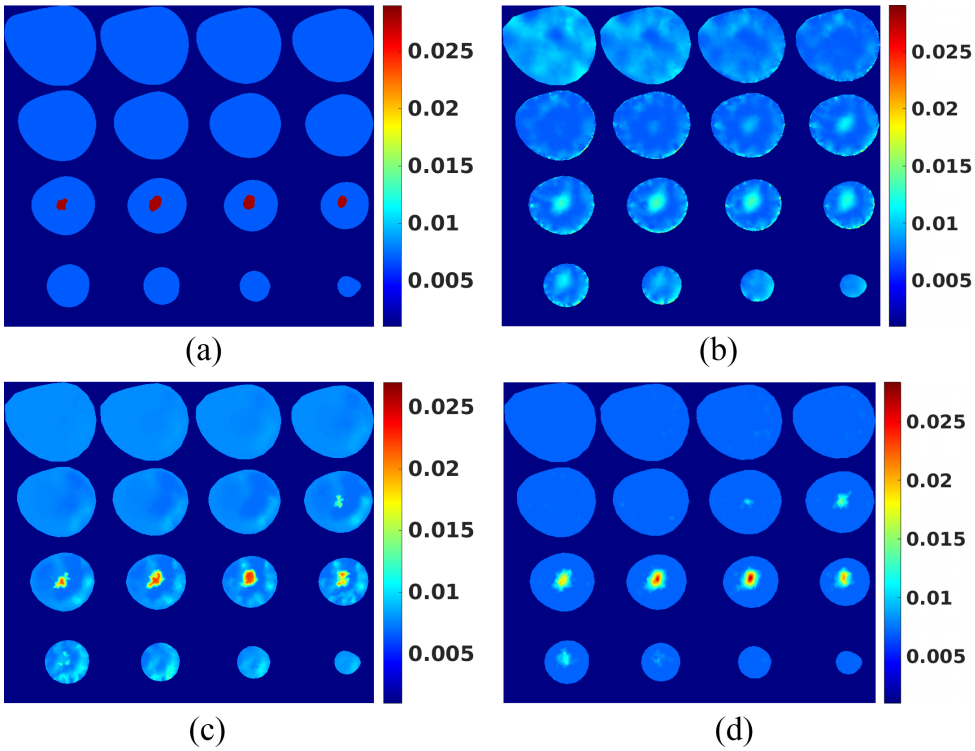

Figure 7. Reconstructed absorption coefficient images using the clinical breast CT image as anatomical guidance with (a) the ground truth image; (b) without the structural guidance; (c) the soft prior method and (d) the kernel method.

3.2 Phantom experimental results

An agar phantom experiment with one target was conducted to evaluate the proposed kernel method. Phantom geometries and the DOT prototype system are described in section 2.4. Fig. 3(b) shows a cross section of the phantom CT image obtained from the dedicated breast cancer CT scanner. As described in the numerical simulation, we have performed the DOT reconstruction of this phantom experiment without the structural prior, with the structural prior through the method of soft prior, and with the structural guidance by the proposed kernel method of 12 different cases with 3 different nearest neighbor k (16, 32, 64) and 4 different voxel numbers (3×3×3, 5×5×5, 7×7×7, and 9×9×9). The reconstructed optical absorption coefficient images are plotted in Fig. 8(a) for the case without the structural guidance, Fig. 8(b), for the soft prior case, and Fig. 8(c) for the kernel method with k=64 and a voxel number of 7×7×7. Fig. 8(c) is the best case among all the 12 cases of the kernel method. Fig. 8(a) indicates that the target is missed for the DOT reconstruction without any structural guidance. From Fig. 8(b), we see that the target is reconstructed at the right location, but the maximum value of absorption coefficients inside the target region is less than the true value. As indicated by Fig. 8(c), the kernel method with k=64 and the voxel number of 7×7×7 has a good reconstructed image. We calculated the image quality metrics for the results in Fig. 8 and listed those in Table 6, from which we know that the reconstructed image with the soft prior method has the best metrics as we see in the numerical simulations. The main reason is that we extracted the target and background regions accurately from the CT image and did not add any segmentation error in the soft prior guidance. However, the optical absorption coefficients in the target region are less than the true value. The kernel method reconstruction has the comparable results with the soft prior method in terms of the image evaluation metrics and has slightly better accuracy of the reconstructed value in the target region than the soft prior method.

Table 6. For the phantom experiment, the calculated VR, Dice, and CNR for images in Fig. 9.

	VR	Dice	CNR
No prior	0.87	0.0	0.48
Soft prior	1.0	1.0	246.20
Kernel method	0.65	0.76	16.03

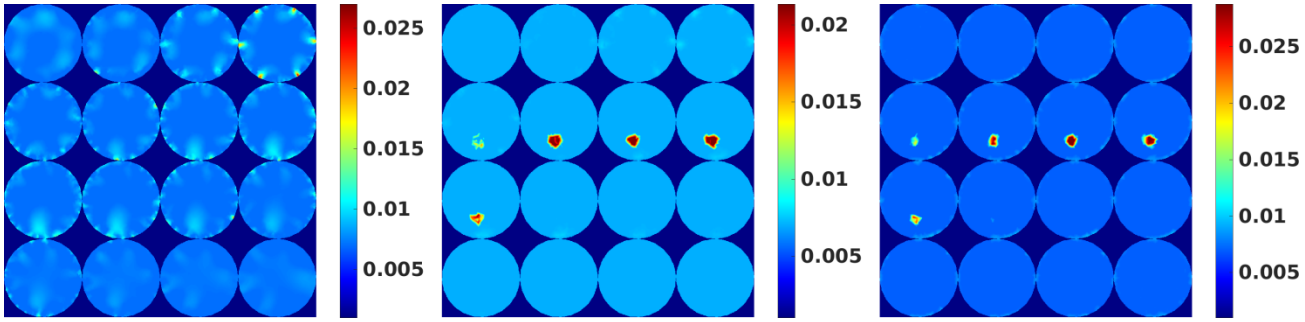

Figure 8. Reconstructed DOT images of the phantom experiment: (a) without the structural guidance; (b) with the structural guidance through the soft prior method; (c) with the structural guidance by the kernel method (k=64, voxel number 7×7×7)

4. DISCUSSIONS AND CONCLUSION

We proposed a kernel method to incorporate the anatomical guidance into the DOT image reconstruction. Compared with the conventional structural prior guided DOT reconstruction algorithms, such as soft prior, the proposed method has the advantages of not requiring image segmentation and region classification as demonstrated by Fig. 7. With the correct guidance as shown in Fig. 4 the soft prior outperforms the proposed kernel method with better VR and DICE coefficient. However, the proposed methods yields higher optical absorption coefficients in the numerical simulation with breast CT data and phantom experiment. It also yields less artifacts near the source locations than the soft prior method as shown in Fig. 7. Key parameters in this proposed method are the voxel number and *k*-nearest neighbor. From the simulation study, we can see that *k*-nearest neighbor has signification impact to improve the quality of reconstructed image. However, voxel numbers are not changing the quality of the reconstructed images significantly, while increasing the computation time. In this study, we conclude *k*-nearest neighbor as k=64 and voxel number of 7×7×7 as optimum parameter.

In this study, we validated the proposed kernel method with both numerical simulations and phantom experiments. But we only reconstruct the absorption coefficient images because our initial project goal is to reconstruct the hemoglobin concentration that is closely related to the absorption coefficient. We believe our current study is sufficient to validate the proposed kernel method, whereas in the future we will apply the kernel method to reconstruct both the optical absorption and the reduced scattering coefficient images.

The proposed kernel method is validated by the CT image guidance. It is straightforward to apply the proposed kernel method for DOT imaging with other anatomical guidance such as MRI [61,62]. We have studied the simultaneous PET and fluorescence molecular tomography (FMT) imaging for studies with mice model [63]. The proposed kernel method can potentially be applied to PET-guided DOT for breast cancer molecular imaging because a breast dedicated PET scanner has a spatial resolution of about 2.5 mm, which is higher than that of the DOT imaging [64].

In summary, simulation and phantom experiment results have validated the kernel method. Our results indicate that the higher number of nearest neighbors and the larger voxel size improve the quality of the reconstructed images. The numerical simulation results indicate that the proposed kernel method is robust to CT contrast and the false positive targets in the guided CT image. With the clinical breast CT image, we demonstrated that we do not need image segmentation for the kernel method. Future work includes investigating the effects of false negative prior information in anatomical images on the performance of the proposed method. Moreover, a thorough examination of this method with a clinical DOT measurement data will be conducted in the future.

5. ACKNOWLEDGMENT

Authors thank research support from California Breast Cancer Research Program (IDEA: 20IB-0125), the startup fund from UC Merced, and the summer fellowship from the graduate program of Biological Engineering and Small Technologies (BEST), School of Engineering, UC Merced. Authors thank Professor Ramsey D. Badawi in Department of Radiology, UC Davis for discussion.

REFERENCES

[1] Yodh, A. and Chance, B., "Spectroscopy and imaging with diffusing light," *Physics Today* **48**(3), 34–41(1995). [doi:10.1063/1.881445].

[2] Boas, D. A., Brooks, D. H., Miller, E. L., DiMarzio, C. A., Kilmer, M., Gaudette, R. J., and Zhang, Q., "Imaging the body with diffuse optical tomography," *IEEE Signal Processing Magazine* **18**(6), 57–75 (2001). [doi:10.1109/79.962278].

[3] Pogue, B., Testorf, M., McBride, T., Osterberg, U., and Paulsen, K., "Instrumentation and design of a frequency-domain diffuse optical tomography imager for breast cancer detection," *Optics Express* **1**(13), 391–403 (1997). [doi:10.1364/OE.1.000391].

[4] Carpenter, C. M., Pogue, B. W., Jiang, S., Dehghani, H., Wang, X., Paulsen, K. D., Wells, W. A., Forero, J., Kogel, C., Weaver, J. B., et al., "Image-guided optical spectroscopy provides molecular-specific information in vivo: MRI-guided spectroscopy of breast cancer hemoglobin, water, and scatterer size," *Optics Letters* **32**(8), 933–935 (2007). [doi:10.1364/OL.32.000933].

[5] Li, C., Zhao, H., Anderson, B., and Jiang, H., "Multispectral breast imaging using a ten-wavelength, 64×64 source/detector channels silicon photodiode-based diffuse optical tomography system," *Medical Physics* **33**(3), 627–636 (2006). [doi:10.1118/1.2171508].

[6] Hebden, J. C., Gibson, A., Yusof, R. M., Everdell, N., Hillman, E. M., Delpy, D. T., Arridge, S. R., Austin, T., Meek, J. H., and Wyatt, J. S., "Three-dimensional optical tomography of the premature infant brain," *Physics in Medicine and Biology* **47**(23), 4155–4166 (2002). [doi:10.1088/0031-9155/47/23/303].

[7] Boas, D. A., Dale, A. M., and Franceschini, M. A., "Diffuse optical imaging of brain activation: approaches to optimizing image sensitivity, resolution, and accuracy," *Neuroimage* **23**, S275–S288 (2004). [doi:10.1016/j.neuroimage.2004.07.011].

[8] Chitnis, D., Cooper, R. J., Dempsey, L., Powell, S., Quaggia, S., Highton, D., Elwell, C., Hebden, J. C., and Everdell, N. L., "Functional imaging of the human brain using a modular, fibre-less, high-density diffuse optical tomography system," *Biomedical Optics Express* **7**(10), 4275–4288 (2016). [doi:10.1364/BOE.7.004275].

[9] Ntziachristos, V., Yodh, A., Schnall, M., and Chance, B., "Concurrent MRI and diffuse optical tomography of breast after indocyanine green enhancement," *Proceedings of the National Academy of Sciences* **97**(6), 2767–2772 (2000). [doi:10.1073/pnas.040570597].

[10] Choe, R., Konecky, S. D., Corlu, A., Lee, K., Durduran, T., Busch, D. R., Pathak, S., Czerniecki, B. J., Tchou, J., Fraker, D. L., et al., "Differentiation of benign and malignant breast tumors by in-vivo threedimensional parallel-plate diffuse optical tomography," *Journal of Biomedical Optics* **14**(2), 024020 (2009). [doi:10.1117/1.3103325].

[11] Li, C. and Jiang, H., "Imaging of particle size and concentration in heterogeneous turbid media with multispectral diffuse optical tomography," *Optics Express* **12**(25), 6313–6318 (2004). [doi:10.1364/OPEX.12.006313].

[12] Li, C., Grobmyer, S., Massol, N., Liang, X., Zhang, Q., Chen, L., Fajardo, L., and Jiang, H., "Noninvasive in vivo tomographic optical imaging of cellular morphology in the breast: possible convergence of microscopic pathology and macroscopic radiology.," *Medical Physics* **35**(6), 2493–2501 (2008). [doi:10.1118/1.2921129].

[13] Grosenick, D., Rinneberg, H., Cubeddu, R., and Taroni, P., "Review of optical breast imaging and spectroscopy," *Journal of Biomedical Optics* **21**(9), 091311 (2016). [doi:10.1117/1.JBO.21.9.091311].

[14] Jiang, Z., Piao, D., Xu, G., Ritchey, J. W., Holyoak, G. R., Bartels, K. E., Bunting, C. F., Slobodov, G., and Krasinki, J. S., "Trans-rectal ultrasound-coupled near-infrared optical tomography of the prostate part II: Experimental demonstration," *Optics Express* **16**(22), 17505–17520 (2008). [doi:10.1364/OE.16.017505].

[15] Piao, D., Bartels, K. E., Jiang, Z., Holyoak, G. R., Ritchey, J. W., Xu, G., Bunting, C. F., and Slobodov, G., "Alternative transrectal prostate imaging: a diffuse optical tomography method," *IEEE Journal of Selected Topics in Quantum Electronics* **16**(4), 715–729 (2010). [doi:10.1109/JSTQE.2009.2034026].

[16] He, J., Wilson, B. C., Piao, D., and Weersink, R., "Diffuse optical tomography to monitor the photocoagulation front during interstitial photothermal therapy: Numerical simulations and measurements in tissue-simulating phantoms," *Photonics & Lasers in Medicine* **3**(3), 241–254 (2014). [doi:10.1515/plm-2014-0011].

[17] Weersink, R. A., Chaudhary, S., Mayo, K., He, J., and Wilson, B. C., "Shape-based reconstruction for transrectal diffuse optical tomography monitoring of photothermal focal therapy of prostate cancer: simulation studies," *Journal of Biomedical Optics* **22**(4), 045004 (2017). [doi:10.1117/1.JBO.22.4.045004].

[18] Xu, Y., Iftimia, N., Jiang, H., Key, L., and Bolster, M., "Imaging of in vitro and in vivo bones and joints with continuous-wave diffuse optical tomography," *Optics Express* **8**(7), 447–451 (2001).[doi:10.1364/OE.8.000447].

[19] Yuan, Z., Zhang, Q., Sobel, E. S., and Jiang, H., "Tomographic x-ray–guided three-dimensional diffuse optical tomography of osteoarthritis in the finger joints," *Journal of Biomedical Optics* **13**(4), 044006 (2008). [doi:10.1117/1.2965547].
[20] Arridge, S. R., "Optical tomography in medical imaging," *Inverse Problems* **15**(2), R41–R93 (1999). [doi:10.1088/0266-5611/15/2/022].
[21] Pei, Y., Graber, H. L., and Barbour, R. L., "Normalized–constraint algorithm for minimizing inter–parameter crosstalk in DC optical tomography," *Optics Express* **9**(2), 97–109 (2001). [doi:10.1364/OE.9.000097].
[22] Cao, N., Nehorai, A., and Jacob, M., "Image reconstruction for diffuse optical tomography using sparsity regularization and expectation-maximization algorithm," *Optics Express* **15**(21), 13695–13708 (2007). [doi:10.1364/OE.15.013695].
[23] Dehghani, H., Eames, M. E., Yalavarthy, P. K., Davis, S. C., Srinivasan, S., Carpenter, C. M., Pogue, B. W., and Paulsen, K. D., "Near infrared optical tomography using NIRFAST: Algorithm for numerical model and image reconstruction," *International Journal for Numerical Methods in Biomedical Engineering* **25**(6), 711–732 (2009). [doi:10.1002/cnm.1162].
[24] Niu, H., Tian, F., Lin, Z.-J., and Liu, H., "Development of a compensation algorithm for accurate depth localization in diffuse optical tomography," Optics Letters 35(3), 429–431 (2010). [doi:10.1364/OL.35.000429].Lee, O., Kim, J. M., Bresler, Y., and Ye, J. C., "Compressive diffuse optical tomography: noniterative exact reconstruction using joint sparsity," *IEEE transactions on medical imaging* **30**(5), 1129–1142 (2011). [doi:10.1109/TMI.2011.2125983].
[25] Lee, O., Kim, J. M., Bresler, Y., and Ye, J. C., "Compressive diffuse optical tomography: noniterative exact reconstruction using joint sparsity," *IEEE transactions on medical imaging* **30**(5), 1129–1142 (2011). [doi:10.1109/TMI.2011.2125983].
[26] Prakash, J., Shaw, C. B., Manjappa, R., Kanhirodan, R., and Yalavarthy, P. K., "Sparse recovery methods hold promise for diffuse optical tomographic image reconstruction," *IEEE Journal of Selected Topics in Quantum Electronics* **20**(2), 74–82 (2014). [doi:10.1109/JSTQE.2013.2278218].
[27] Prakash, J., Dehghani, H., Pogue, B. W., and Yalavarthy, P. K., "Model-resolution-based basis pursuit deconvolution improves diffuse optical tomographic imaging," *IEEE Transactions on Medical Imaging* **33**(4), 891–901 (2014). [doi:10.1109/TMI.2013.2297691].
[28] Yamashita, O., Shimokawa, T., Aisu, R., Amita, T., Inoue, Y., and Sato, M.-a., "Multi-subject and multitask experimental validation of the hierarchical bayesian diffuse optical tomography algorithm," *NeuroImage* **135**, 287–299 (2016). [doi:10.1016/j.neuroimage.2016.04.068].
[29] Bhowmik, T., Liu, H., Ye, Z., and Oraintara, S., "Dimensionality reduction based optimization algorithm for sparse 3-D image reconstruction in diffuse optical tomography," *Scientific Reports* **6**, 22242 (2016). [doi:10.1038/srep22242].
[30] Shaw, C. B., Li, Z., Pogue, B. W., and Yalavarthy, P. K., "Direct sensitivity based data-optimization strategy for image-guided diffuse optical tomography," *IEEE Journal of Selected Topics in Quantum Electronics* **22**(3), 69–77 (2016). [doi:10.1109/JSTQE.2016.2558178].
[31] Sun, Z., Wang, Y., Jia, K., and Feng, J., "Comprehensive study of methods for automatic choice of regularization parameter for diffuse optical tomography," *Optical Engineering* **56**(4), 041310–041310 (2017). [doi:10.1117/1.OE.56.4.041310].
[32] Schweiger, M., Arridge, S. R., and Nissil¨a, I., "Gauss–Newton method for image reconstruction in diffuse optical tomography," *Physics in Medicine and Biology* **50**(10), 2365–2386 (2005). [doi:10.1088/0031-9155/50/10/013].
[33] Corlu, A., Choe, R., Durduran, T., Lee, K., Schweiger, M., Arridge, S. R., Hillman, E. M., and Yodh, A. G., "Diffuse optical tomography with spectral constraints and wavelength optimization," *Applied Optics* **44**(11), 2082–2093 (2005). [doi:10.1364/AO.44.002082].
[34] Pogue, B. W. and Paulsen, K. D., "High-resolution near-infrared tomographic imaging simulations of the rat cranium by use of a priori magnetic resonance imaging structural information," *Optics Letters* **23**(21), 1716–1718 (1998). [doi:10.1364/OL.23.001716].
[35] Brooksby, B., Jiang, S., Dehghani, H., Pogue, B. W., Paulsen, K. D., Weaver, J., Kogel, C., and Poplack, S. P., "Combining near-infrared tomography and magnetic resonance imaging to study in vivo breast tissue: implementation of a Laplacian-type regularization to incorporate magnetic resonance structure," *Journal of Biomedical Optics* **10**(5), 051504 (2005). [doi:10.1117/1.2098627].
[36] Zhao, Y., Mastanduno, M. A., Jiang, S., Fadi, E.-G., Gui, J., Pogue, B. W., and Paulsen, K. D., "Optimization of image reconstruction for magnetic resonance imaging–guided near-infrared diffuse optical spectroscopy in breast," *Journal of Biomedical Optics* **20**(5), 056009 (2015). [doi:10.1117/1.JBO.20.5.056009].

[37] Ntziachristos, V., Ma, X., and Chance, B., "Time-correlated single photon counting imager for simultaneous magnetic resonance and near-infrared mammography," *Review of Scientific Instruments* **69**(12), 4221–4233 (1998). [doi:10.1063/1.1149235].
[38] Ntziachristos, V., Yodh, A., Schnall, M. D., and Chance, B., "MRI-guided diffuse optical spectroscopy of malignant and benign breast lesions," *Neoplasia* **4**(4), 347–354 (2002). [doi:10.1038/sj.neo.7900244].
[39] Zhu, Q., Cronin, E. B., Currier, A. A., Vine, H. S., Huang, M., Chen, N., and Xu, C., "Benign versus malignant breast masses: Optical differentiation with US-guided optical imaging reconstruction," *Radiology* **237**(1), 57–66 (2005). [doi:10.1148/radiol.2371041236].
[40] Zhu, Q., Tannenbaum, S., and Kurtzman, S. H., "Optical tomography with ultrasound localization for breast cancer diagnosis and treatment monitoring," *Surgical Oncology Clinics of North America* **16**(2), 307–321 (2007). [doi:10.1016/j.soc.2007.03.008].
[41] Xu, Y. and Zhu, Q., "Estimation and imaging of breast lesions using a two-layer tissue structure by ultrasound-guided optical tomography," Journal of Biomedical Optics 20(6), 066002 (2015). [doi:10.1117/1.JBO.20.6.066002].
[42] Fang, Q., Carp, S. A., Selb, J., Boverman, G., Zhang, Q., Kopans, D. B., Moore, R. H., Miller, E. L., Brooks, D. H., and Boas, D. A., "Combined optical imaging and mammography of the healthy breast: optical contrast derived from breast structure and compression," *IEEE transactions on medical imaging* **28**(1), 30–42 (2009). [doi:10.1109/TMI.2008.925082].
[43] Fang, Q., Selb, J., Carp, S. A., Boverman, G., Miller, E. L., Brooks, D. H., Moore, R. H., Kopans, D. B., and Boas, D. A., "Combined optical and X-ray tomosynthesis breast imaging," *Radiology* **258**(1), 89–97 (2011). [doi:10.1148/radiol.10082176].
[44] Yalavarthy, P. K., Pogue, B. W., Dehghani, H., and Paulsen, K. D., "Weight-matrix structured regularization provides optimal generalized least-squares estimate in diffuse optical tomography," *Medical Physics* **34**(6), 2085–2098 (2007). [doi:10.1118/1.2733803].
[45] Phaneendra K Yalavarthy, Brian W Pogue, Hamid Dehghani, Colin M Carpenter, Shudong Jiang, and Keith D Paulsen. Structural information within regularization matrices improves near infrared diffuse optical tomography. Opt. Express, 15(13):8043–8058, 2007. [doi:10.1364/OE.15.008043].
[46] Zhang, L., Zhao, Y., Jiang, S., Pogue, B. W., and Paulsen, K. D., "Direct regularization from co-registered anatomical images for MRI-guided near-infrared spectral tomographic image reconstruction," *Biomedical Optics Express* **6**(9), 3618–3630 (2015). [doi:10.1364/BOE.6.003618].
[47] Feng, J., Jiang, S., Xu, J., Zhao, Y., Pogue, B. W., and Paulsen, K. D., "Multiobjective guided priors improve the accuracy of near-infrared spectral tomography for breast imaging," *Journal of Biomedical Optics* **21**(9), 090506 (2016). [doi:10.1117/1.JBO.21.9.090506].
[48] Althobaiti, M., Vavadi, H., and Zhu, Q., "Diffuse optical tomography reconstruction method using ultrasound images as prior for regularization matrix," *Journal of Biomedical Optics* **22**(2), 026002 (2017). [doi:10.1117/1.JBO.22.2.026002].
[49] Wang, G. and Qi, J., "PET Image Reconstruction Using Kernel Method," *IEEE Transactions on Medical Imaging* **34**(1), 61–71 (2015). [doi:10.1109/tmi.2014.2343916].
[50] Robert W Holt, Scott Davis, and Brian W Pogue. Contrast difference images can be used to improve fluorescence recovery with drift. In Biomedical Optics, pages BM3A–80. Optical Society of America, 2014. [doi:10.1364/BIOMED.2014.BM3A.80].
[51] Wang, G. and Qi, J., "PET image reconstruction using kernel method," in [2013 IEEE 10th International Symposium on Biomedical Imaging], 1162–1165, IEEE (2013). [doi:10.1109/ISBI.2013.6556686].
[52] Hutchcroft, W., Wang, G., Chen, K. T., Catana, C., and Qi, J., "Anatomically-aided PET reconstruction using the kernel method," *Physics in Medicine and Biology* **61**(18), 6668–6683 (2016). [doi:10.1088/0031-9155/61/18/6668].
[53] Berlinet, A. and Thomas-Agnan, C., [Reproducing Kernel Hilbert Spaces in Probability and Statistics], Springer Science (2004). [doi:10.1007/978-1-4419-9096-9].
[54] Hofmann, T., Schölkopf, B., and Smola, A. J., "Kernel methods in machine learning," *The Annals of Statistics* **36**(3), 1171–1220 (2008). [doi:10.1214/009053607000000677].
[55] Zhu, D. and Li, C., "Nonconvex regularizations in fluorescence molecular tomography for sparsity enhancement," *Physics in Medicine and Biology* **59**(12), 2901–2912 (2014). [doi:10.1088/0031-9155/59/12/2901].
[56] Zhu, D., Zhao, Y., Baikejiang, R., Yuan, Z., and Li, C., "Comparison of regularization methods in fluorescence molecular tomography," *Photonics* **1**(2), 95–109 (2014). [doi:10.3390/photonics1020095].

[57] Baikejiang, R., Zhang, W., and Li, C., "Diffuse optical tomography for breast cancer imaging guided by computed tomography: A feasibility study," *Journal of X-Ray Science and Technology* **25**(3), 341–355(2017) [doi:10.3233/XST-16183].
[58] Li, C. and Jiang, H., "A calibration method in diffuse optical tomography," *Journal of Optics A: Pure and Applied Optics* **6**(9), 844–852 (2004). [doi:10.1088/1464-4258/6/9/005].
[59] Boone, J. M., Kwan, A. L., Yang, K., Burkett, G. W., Lindfors, K. K., and Nelson, T. R., "Computed Tomography for Imaging the Breast," *Journal of Mammary Gland Biology and Neoplasia* **11**(2), 103–111(2006). [doi:10.1007/s10911-006-9017-1].
[60] Baikejiang, R., Zhang, W., Zhu, D., and Li, C., "CT guided diffuse optical tomography for breast cancer imaging," *Proc. SPIE* **9788**, 97882K (2016). [doi:10.1117/12.2216402].
[61] Brooksby, B. A., Dehghani, H., Pogue, B. W., and Paulsen, K. D., "Near-infrared (NIR) tomography breast image reconstruction with a priori structural information from MRI: algorithm development for reconstructing heterogeneities," *IEEE Journal of Selected Topics in Quantum Electronics* **9**(2), 199–209(2003). [doi:10.1109/JSTQE.2003.813304].
[62] Brooksby, B., Jiang, S., Dehghani, H., Pogue, B. W., Paulsen, K. D., Kogel, C., Doyley, M., Weaver, J. B., and Poplack, S. P., "Magnetic resonance-guided near-infrared tomography of the breast," *Review of Scientific Instruments* **75**(12), 5262–5270 (2004). [doi:10.1063/1.1819634].
[63] Li, C., Yang, Y., Mitchell, G. S., and Cherry, S. R., "Simultaneous PET and multispectral 3-Dimensional fluorescence optical tomography imaging system," *Journal of Nuclear Medicine* **52**(8), 1268–1275 (2011). [doi:10.2967/jnumed.110.082859].
[64] Wu, Y., Bowen, S. L., Yang, K., Packard, N., Fu, L., Burkett Jr, G., Qi, J., Boone, J. M., Cherry, S. R., and Badawi, R. D., "PET characteristics of a dedicated breast PET/CT scanner prototype," *Physics in Medicine and Biology* **54**(13), 4273 (2009). [doi:10.1088/0031-9155/54/13/020].